# Permeability evolution during fluid-pressure induced shear slip in saw-cut and natural granite fractures

Zhiqiang Li[a,b,c], Xiaodong Ma[b,c], Xiang-Zhao Kong[b], Martin O. Saar[b,d], Daniel Vogler[b]

[a] *Shandong University, Geotechnical and Structural Engineering Research Center, 250061 Jinan, Shandong, China*
[b] *ETH Zurich, Geothermal Energy and Geofluids Group, Institute of Geophysics, Department of Earth Sciences, 8092 Zurich, Switzerland*
[c] *ETH Zurich, Swiss Competence Center for Energy Research-Supply of Electricity (SCCER-SoE), 8092 Zurich, Switzerland*
[d] *University of Minnesota, Department of Earth and Environmental Sciences, Minneapolis, USA*

**Abstract**

Subsurface engineering applications, such as the development of enhanced geothermal systems and unconventional oil and gas reservoirs, and the geologic disposal of $CO_2$ and waste water, involve fluid injection into the rock masses deep underground. Elevated fluid pressure can trigger shear slip(s) of pre-existing natural fractures, resulting in permeability changes. The mechanism of slip-induced permeability variation, however, is still not fully understood, and the permeability evolution associated with multiple slips is even more complex. We therefore performed laboratory experiments to investigate the fracture permeability evolution induced by shear slip in both saw-cut and natural fractures with rough surfaces. Our experiments show that the triggering fluid pressures required to induce slip in natural fractures are larger than in saw-cut fractures, likely due to the rougher surface of the natural fractures. We further observe that a critical shear displacement dominates the permeability evolution. When the accumulative shear displacement reaches the critical shear displacement, we find an initial permeability increase for natural fractures, followed by a permeability decrease after the most significant slip event. For the saw-cut fractures, the first slip shows the largest shear displacement and related permeability change, while further slips result in diminishing displacements. From the beginning to the end of all experiments, no consistent permeability increase or decrease is observed. Although the change of the fracture surface was not measured quantitatively, we found gouge material after rinsing each natural sample. To this end, we at-

*Corresponding author
**Corresponding author
*Email addresses:* xiama@ethz.ch (Xiaodong Ma), davogler@ethz.ch (Daniel Vogler)

tribute the slip-induced permeability evolution to the relationship between the damage of the main asperities, which decreases permeability, and the scale of the shear displacement, which increases permeability through shear dilation.

*Keywords:* hydraulic stimulation, permeability evolution, fractures, granite, shear slip, fracture fluid flow

## 1. Introduction

Subsurface engineering for energy and resources development as well as environmental applications typically involve fluid injection into the rock masses deep underground. Examples include hydraulic stimulation for enhanced geothermal systems [1, 2, 3] and unconventional oil and gas reservoirs [4], geologic disposal of waste water [5] and $CO_2$ [6, 7]. These applications generally result in elevated fluid pressures to various degrees. This leads to a reduction of the effective stress on pre-existing faults and fractures, which may potentially induce shear slip [8]. Several field investigations have indicated that such shear slip can significantly change fracture permeability and thus affect fluid flow in the reservoir and associated solute and heat transport characteristics [9, 10].

Fracture permeability is generally dominated by the fracture aperture, which is known to be strongly influenced by the applied normal stress and shear deformation [11, 12, 13, 14, 15, 16, 17, 18, 19]. A number of experimental studies have shown that the fracture aperture increases with decreasing effective normal stress, leading to an increase in fracture permeability [20, 21, 22, 23, 24, 25, 26]. These observations are consistent with several empirical and theoretical models [27, 28, 29, 22] that correlate the fracture aperture and normal closure to the given normal stress [13, 14, 16, 30].

Besides normal deformation, shear deformation can also lead to significant changes in fracture permeability [31, 32, 33, 34, 35, 36, 37, 38, 39]. These permeability changes can occur in form of permeability increase, due to an increase in aperture by shear dilation, or permeability decrease, due to gouge formation and clogging of the fracture. Shear-induced dilation can result in an increase in the fracture aperture, which can enhance fracture permeability. Different degrees of shear displacement can significantly change the fracture aperture field [33, 40, 38]. Even small shear displacements can result in significant changes in the fracture contact area [39], which affects the fracture's effective fluid flow path and aperture, and consequently permeability. Once shear displacement reaches a certain threshold, previous laboratory observations have shown that permeability tends to stagnate [32]. However, shear deformation can modify fracture surface morphology, which

is exemplified by irreversible deformation of the asperities and/or the production of gouge materials, that can clog flow channels and subsequently decrease fracture permeability [41, 19, 34, 35]. Such permanent changes alter the fracture roughness and aperture, both affecting the fracture permeability. Concerning repeated shear slips on the same fracture, both reversible and irreversible deformations are important for the evolution of permeability [40]. Previous studies thereby clearly highlight the complicated impact of shear slip induced fracture shear dilation and gouge material formation on permeability.

To investigate how the fracture permeability changes due to shear slip, so-called 'shear-flow' experiments have been performed on fractured specimens of various rock types (granite, shale, marble, etc.) [42, 31, 32, 19, 43, 35, 36, 39]. However, the relationship between shear slip and fracture permeability is still not fully understood, likely because the latter is influenced by the complicated interplay of various factors, such as normal stress, fracture surface mating, slip history, fracture size, and shear strength [44, 34, 36]. In most of these shear-flow experiments, the shear slip was enabled by a piston motion [45, 43, 34, 35, 46], which actively regulates the slip velocity and displacement. This allows for the characterization of the resulting friction and permeability changes and the associated seismic attributes. Causing shear slip in such a direct manner (i.e., forced by a piston) can be understood by the increase in shear stress on the fracture. Alternatively, shear slip can also be triggered indirectly by reducing the effective normal stress, or simply by increasing the fluid pressure. To some extent, the latter (i.e., an indirect manner) more closely resembles the in-situ processes acting in faults/fractures on which slip is re-activated by fluid injection. Although elevated fluid pressures may also modify the shear stresses on the fractures, the fracture slip, or re-activation, should be primarily attributed to the reduction of the effective normal stress, essentially "unclamping" the fault/fracture [47, 48].

In this paper, we describe a series of laboratory experiments on rock cores that follow this indirect manner of inducing shear slip, i.e., by reducing the effective normal stress. In these experiments, the fluid pressure in the fracture is slowly raised until slip is induced. We repeat this triggering process several times to enable the investigation of the evolution of the slip behavior and associated permeability changes. We measure the permeability in both saw-cut and naturally fractured granite specimens under constant normal stress and fluid pressure levels, so that the permeability evolution can be, in principle, attributed to the morphological changes of the fracture surfaces.

## 2. Methods

### *2.1. Specimens and preparation*

We conducted the shear-flow experiments on granite rock cores from the Grimsel Test Site in Switzerland. The cores were cylinders with a diameter of 25.4 mm and a length of 50.8 mm. All six specimens contained a through-going fracture along their long axis (Figure 1). Three of the specimens contained a natural fracture that was overcored from a larger rock core sample, while the other three specimens contained saw-cut fractures that were polished to a specified roughness. A list of specimens and their physical properties is provided in Table 1.

The specimens were carefully prepared and instrumented before being inserted into the pressure vessel. To enable shear displacement along a specimen's axial direction, we allowed room for the opposite sides of the fracture to offset, should shear slip occur. An approximately 7-8 mm long section was cut off from each half of the specimen and the two cut-off sections were located on opposite ends of the fracture (Figure 1c). This configuration keeps opposite sides of the fracture surfaces mated, especially in natural specimens. The two cut-off rock sections were replaced with 3D-printed rubber spacers (90 Shore hardness, see Figure 1c). The deformable rubber spacers, once axially compressed in the pressure vessel, enable the accumulation of shear stress on the fracture until fluid-pressure induced slip occurs along the fracture (Figure 1c), while preventing collapse of the rubber jacket enclosing the specimen. The rubber spacers also act as place holders between the specimen and the piston under confinement during the experiments.

The fracture surfaces of the saw-cut specimens were polished to different finishes, i.e., by sandpaper of 80, 240, and 400 grit. The fracture surfaces were polished against a fixed sandpaper along the direction perpendicular to the cores' axial direction (i.e., the fluid flow direction as detailed later) with a steady motion for 10 minutes. The surface roughness of the natural fractures was characterized by photogrammetric scanning prior to the shear-flow experiments. Analysis of the photogrammetric scan images yields the average roughness of opposite fracture surfaces. The Z2 and Joint Roughness Coefficient (JRC) indexes and standard deviation of 20 surface height profiles along the specimen axis were obtained from each fracture surface (see Appendix A for details). The roughness of these natural fractures was also measured at smaller scales by zooming to 1 cm$\times$1 cm patches of the fracture surfaces and averaging across these patches. Figure 2 shows the quantified roughness values in terms of both Z2 and JRC indexes. Details regarding the computation of each roughness metric can be found in previous publications [49, 50, 51].

According to the smaller-scale measurements, Specimen N27 (tensile fracture mode) exhibits the greatest roughness, while Specimen N03 (mixed tensile and shear fracture mode) is the smoothest. The quantified roughness of Specimen N21 (shear fracture mode) is ambiguous. According to Z2 or JRC indexes, N21 exhibits a roughness similar to that of Specimen N03, while the roughness, indicated by the measured standard deviation, is more similar to the larger roughness found for Specimen N27. When smaller scales are investigated on patches of 1 cm×1 cm, however, the roughness metrics are more aligned, with increasing roughness values from Specimen N03 to N21 to N27.

### *2.2. Experimental apparatus*

The specimen is hosted in a pressure vessel and subjected to a triaxial state of stress ($\sigma_1 > \sigma_2 = \sigma_3$), as well as internal fluid pressure acting within the fracture. Confining pressure, $\sigma_c$, axial stress, $\sigma_A$, fluid inlet pressure, $P_{in}$, and fluid outlet pressure, $P_{out}$, are each independently controlled by individual syringe pumps (pressure ranges of up to 100 MPa and 0.1% full-scale accuracy) and continuously recorded (at a sampling rate of 1/3 Hz)[52, 53, 54, 7, 55]. A displacement gauge (0.5 $\mu$m resolution) is affixed to the upper end-cap to capture its axial movement. The axial displacement in the instrumented specimen is obtained after subtracting the end-cap deformation from the total measured displacement. We attribute the measured axial displacement to the shear-slip displacement across the fracture, since the fracture is parallel to the specimen axis (coinciding with the shear direction). For the same reason, the normal stress, $\sigma_n$, on the fracture is equal to the confining pressure, $\sigma_c$. We did not consider the contribution of specimen shortening to the shear displacement, because the axial strain, due to the applied load, is negligible.

### *2.3. Experimental procedure*

After the specimen has been prepared and inserted into the pressure vessel, the entire apparatus is vacuumed down to 0.02 MPa, while the normal and axial stresses are both kept at 1 MPa. Then, the pressure vessel and the specimen are saturated with de-ionized water. As illustrated in Figure 3, the loading path begins with the cyclic loading of both the normal stress and the axial stress, to ensure good mating of the fracture surfaces.

Typically, after the first three cycles, the normal and axial stresses are raised to 3.0 MPa and 6.0 MPa, respectively, and then kept constant thereafter. By trial and error, the above applied

stress levels were determined in order to ensure that slip could be induced at reasonable elevated fluid pressures. For each specimen, a so-called 'starting' fracture permeability, $k_0$ in Figure 3, is measured before the first shear slip takes place. This is followed by a gentle increase in fluid pressure to induce shear slip on the fracture. Both increase and decrease of fluid pressure are driven at a rate of 2.5 kPa/s. When slip occurs, the critical transient fluid pressure is recorded and referred to as the 'triggering pressure,' $P_t$, for that particular slip event.

Upon the detection of a slip event (indicated by a sudden change of axial displacement), the fluid pressure, $P$, is kept constant for approximately 20 minutes to allow the slip to fully settle. The fluid pressure is then lowered back to its starting level of 0.2 MPa.

Before and after each induced slip, the fracture permeability is measured within a 15 minute window. We assume steady-state fluid flow conditions when a constant inlet fluid flow rate of $Q$= 0.5 ml/s and a constant outlet fluid pressure of 0.2 MPa have been reached. The absolute, bulk permeability, $k$, is then averaged from the data recorded during the last 10 minutes. For each specimen, we limit the total number of slip events to four, in order to prevent failure of the rubber spacer. We then obtain the averaged permeability after each shear slip event, $k_i$, with i=1,2,3, and 4, the transient shear displacement step during each slip event, $d_i$, with i=1,2,3, and 4, and the cumulative shear displacement after each slip event, $\sum d_i$, with i=1,2,3, and 4.

## 3. Results

In our experiments, special focus has been placed on the macroscopic characteristics of shear slip. Therefore, the most relevant physical quantities measured are the triggering pressure, $P_t$, considered a proxy for the fracture's frictional strength, shear displacement, $d$, a quantification of the possible degree of shear deformation, and fracture permeability, $k$, a proxy for the extent of fracture morphology changes. Among them, fracture permeability was derived assuming laminar flow through the fractures, using the cubic law (Eq. 1) [11]:

$$k = \frac{1}{12}[-\frac{12\mu l Q}{w(P_{in} - P_{out})}]^{2/3}, \tag{1}$$

where $Q$ is the fluid flow rate, $\mu$ is the fluid dynamic viscosity, and $l$ and $w$ are the length and width of the fracture, respectively.

The experimental results of all specimens are summarized in Table 1. Figure 4 provides a representative overview of the measured physical quantities in a natural fracture and a saw-cut fracture

specimen (N03 and A34), respectively (see Appendix B for results of other specimens). The effect of (quasi-)hydro-static loading during the three mating cycles is inferred from the displacement measurement. The hysteresis of displacement diminished with mating cycles, indicating progressively mated fracture surfaces. The 'effective' displacement measurement began as the axial stress, $\sigma_A$, and normal stress, $\sigma_n$, were raised to the designated levels (6 MPa and 3 MPa, respectively). Then, the 'starting' permeability, $k_0$, was measured for approximately 15 minutes before the first slip event was triggered. At a reasonably elevated fluid pressure (i.e., the triggering pressure, $P_t$), the first slip becomes apparent in the displacement data. Clearly, the majority of the displacement occurs right after the triggered slip (with one exception: Specimen N27), however, we typically allowed $\sim$20 minutes for the shear slip to stabilize. Then, the permeability, $k_1$, was measured during a 15 minute time window. After that, all further triggering slips ($d_2$,$d_3$,and $d_4$), and corresponding post-slip permeability measurements ($k_2$,$k_3$,and $k_4$), were repeated in the same fashion.

While permeability measurements were recorded during the entire experiment, data fluctuations outside the designated 'stable' measurement windows (i.e., $t_4-t_5$, $t_6-t_7$..., as indicated in Figure 3) should be ignored. For example, the permeability curve during the mating cycles, the initiation and the end of individual slip, only reflect transient behaviors, where no long-term permeability measurement under stable conditions was performed. Since the permeability data have include significant noise, we employed a moving average filter, i.e., the mean value in a interval of 45 seconds, to show the trend of permeability variations more clearly; the standard deviation from the average was also calculated to quantify the data noise level (Table 1). Notably, the permeability fluctuations of natural fractures were generally more pronounced than those of the saw-cut fractures. Among the three saw-cut specimens, it appears that the degree of permeability fluctuation increases with fracture roughness (i.e., decreasing grit number).

### *3.1. Triggering pressure*

The triggering pressure, $P_t$, of individual slips is summarized for all specimens in Figure 5a. For all specimens, $P_t$ increases with successive slip events, although the rate of increase declines continuously. Specifically, $P_t$ ranges from 0.47 MPa (A28) to 1.89 MPa (N21) for the 1st shear slip event and 0.81 MPa (A28) to 2.52 MPa (N21) for the 4th slip event. With the exception of one slip event (the 1st slip in N03), natural fracture specimens are associated with $P_t$ of more than 1.0 MPa (and up to 2.52 MPa), while specimens with saw-cut fractures feature $P_t$ no more than

1.0 MPa (Figure 5a). Both the starting value of $P_t$ and its increase from one slip to another are significantly higher in natural fractures than in saw-cut fractures. The smallest starting value of $P_t$ for the natural fractures is that in Specimen N03, and the largest is that in Specimen N21, which does not correlate with fracture roughness. For the saw-cut fractures, the order of the triggering pressure, $P_t$, does negatively correlate with fracture roughness, with the largest $P_t$ found in A34, and the smallest $P_t$ found in A28.

It is worth noting that the order of specimens from highest to lowest $P_t$ does not change with an increase in the number of shear slip events. However, all $P_t$ decrease between sequential slip events, likely caused by reduced surface deformation as the total slip distance increases. Interestingly, in Specimen N27 the decrease of $P_t$ with further slip is noticeably less pronounced than for Specimens N21 and N03, which could lead to larger triggering pressure values given further slip events. Tensile fractures (i.e., N27), which commonly exhibit larger roughness, could therefore be more likely to exhibit strong signs of surface damage, whereas previously sheared fractures are often associated with less surface roughness as they have already experienced significant surface damage [50].

Compared with the saw-cut fractures, the natural fractures, with generally larger roughness values, result in higher $P_t$ (Figure 2). As friction and, consequently, shear strength of the natural fractures become larger, larger forces are required to trigger slip along the interlocked fractures in their initial, mated configuration under the same normal stress. The fact that $P_t$ continuously increases with the number of slip events, for both natural and saw-cut specimens, suggests that shear slip affects the fracture surface morphology, where parts of asperities with relatively weak strength are likely being damaged and are potentially forming ridges that increase the fracture roughness.

### *3.2. Shear displacement*

The evolution of shear displacement, associated with individual slips, $d$, is shown in Figure 5b. Induced slip, $d$, ranges from 0.0185 mm (N03) to 0.0570 mm (N21) for the 1st shear slip event and from 0.0140 mm (A21 and A34) to 0.2775 mm (N27) for the 4th/last shear slip event, without exceeding 0.3 mm. The shear displacements, $d$, of natural fractures are much larger than those of the saw-cut specimens. Note, that the vertical scale of $d$ in Figure 5b differs between natural and saw-cut fractures.

For natural fractures, the shear displacement, associated with the 1st slip event, $d_1$, is the smallest in all slip events. The second slip event, $d_2$, typically exceeds $d_1$, but whether shear displacement increases or decreases in subsequent slip events varies from one specimen to another. After the maximum shear displacement, $d_{max}$, occurred, Specimens N03 and N21 exhibit a decrease in shear displacement ($d_3$ and $d_4$) during subsequent shear slip events. Due to differences in friction among different modes of fractures, the value of each $d$ is quite variable, which has also been reported previously [40].

Observations of the slip distance, $d$, differ for saw-cut fractures and for natural fractures. Saw-cut fractures typically feature the maximum slip distance, $d_{max}$, during the 1st slip. All the saw-cut fractures then experience a sharp decrease in $d$ during the 2nd slip event, followed by moderate changes for subsequent slips events. The saw-cut fractures (A21 and A34) follow a general trend of decreasing $d$ with further slip events, while A28, with the largest roughness (80 grit), shows plateauing slip distances. This suggests that the specimen experiences a strong effect of comminution on the 1st shear slip event for the saw-cut fracture, which increases the frictional stability of the fracture and reduces shear displacement [34, 36].

Overall, for both natural and saw-cut fractures, the triggering pressure, $P_t$, is positively correlated with shear displacement, $d$, (Figure 6). For the natural fracture specimens, $d$ increases significantly with increasing $P_t$, while for the saw-cut specimens, $d$ decreases with increasing $P_t$ (Figure 6).

### *3.3. Permeability*

The permeability evolution with successive slip events for all specimens is shown in Figure 5c. As also summarized in Table 1, $k_0$ of the natural fractures is approximately $12.29 \times 10^{-10}$, $2.58 \times 10^{-10}$, and $2.06 \times 10^{-10}$ m$^2$ for Specimens N03, N21, and N27, respectively. The permeability change for the four slip events is about one order of magnitude (roughly between $10^{-10}$ and $10^{-9}$ m$^2$). Maximum permeability is about $20.57 \times 10^{-10}$ ($+8.28 \times 10^{-10}$) m$^2$, $8.51 \times 10^{-10}$ ($+5.93 \times 10^{-10}$) m$^2$), and $4.74 \times 10^{-10}$ ($+2.68 \times 10^{-10}$) m$^2$ for Specimen N03, N21, and N27, respectively (Figure 5c). For Specimens N03 and N27, the 1st slip causes only a very small permeability change. However, both specimen experience a noticeable permeability increase after the 2nd slip event and monotonically decreasing permeability thereafter. For Specimen N21, the permeability experiences a seemingly sporadic variation across multiple slip events, although the extent of change between slip events gradually diminishes. It is worth noting that the measurements of N21 are associated with

a somewhat higher uncertainty (see error bar in Figure 5c). So, with the exception of the 4th slip event in Specimen N27, the permeability of the natural fractures does not remain constant after the maximum value has been reached (usually after the 1st or 2nd slip event), but decreases again.

Interestingly, the maximum permeability is observed in reverse order to fracture roughness, with the roughest and smoothest fractures (N27 and N03) experiencing the smallest and largest permeability measurements, respectively. The observed increase in permeability is likely caused by shear dilation, where shear displacement causes the mated fracture surfaces to ride up on individual asperities, thereby increasing the fracture aperture and correspondingly the permeability [27, 56]. Furthermore, since $d$ and the associated increase in permeability are quite small, this may imply that the damage of asperities, caused by shear displacement, is limited, but more flow paths developed. Notably, once fractures experience maximum displacement, $d_{max}$, with the exception of Specimen N27, permeability starts to decrease. This might suggest that $d_{max}$ is a sign of permeability reversal.

Initial permeability, $k_0$, of the saw-cut fractures is around $1.65 \times 10^{-10}$ (Specimen A28, 80 grit), $1.09 \times 10^{-10}$ (Specimen A21, 240 grit) and $8.17 \times 10^{-10}$ m$^2$ (Specimen A34, 400 grit). The variation of permeability in saw-cut fractures across multiple slip events is within one order of magnitude (roughly between $10^{-10}$ and $10^{-9}$ m$^2$). The maximum permeability reached (and the associated permeability change in parenthesis) are $3.70 \times 10^{-10}$ ($+2.05 \times 10^{-10}$) (A28), $1.09 \times 10^{-10}$ ($+2.15 \times 10^{-10}$ m$^2$) (A21) and $8.17 \times 10^{-10}$ m$^2$ (no permeability increase) (A34) (Figure 5c). For Specimen A28, after the 1st slip, which corresponds to $d_{max}$, the permeability, $k_1$, increases significantly and reaches its maximum value. Then, permeability decreases gradually with further slip events. For Specimen A34, the 1st slip event, coinciding with $d_{max}$ as well, is also associated with a significant permeability change, however, permeability decreases. Thereafter, permeability plateaued for all further slip events. For Specimen A21, the permeability changes little when subjected to the 1st and 2nd slip events, and the maximum permeability is attained after the 3rd slip.

After the 1st slip event occurs, coinciding with $d_{max}$ in the saw-cut fractures, the associated permeability, $k_1$, change differs from one specimen to another. For example, $k_1$ shows an increase (A28), no apparent change (A21), and a decrease (A34) from $k_0$, with the specimens listed in order of decreasing roughness. After the 1st slip event, the permeability remains almost constant for the rest of the slip events, except for the permeability of Specimen A21, after the 3rd and the 4th

slip events. It appears that the fracture roughness is related to the trend of permeability change. The strong effect of comminution during the initial shear slip is of particular relevance, and its complex effect may lead to different trends of $k_1$. This change of permeability can be attributed to the extremely small asperities in the saw-cut fractures, which prevents larger geometry changes in the fractures after shearing.

For all specimens, the fracture permeability changes up to one order of magnitude after experiencing shear displacement. As shown, the natural fractures exhibit larger slip-associated permeability changes than the saw-cut fractures. This is probably due to the difference in roughness of the natural fractures, and their subsequent change of asperities (surface morphology) during slip. In addition, there is no consistent trend of permeability change, neither for individual slip events nor for the entire experiment set. However, the net permeability change in most of the specimens is practically negligible after several slip events.

## 4. Mechanism of permeability evolution

Based on our observations, the extent of shear slip, $d$, plays an important role in the slip-induced permeability evolution. Figure 7 illustrates the relationship between the derived permeability, $k$, and accumulative shear displacement of each slip event, $\sum d_i$. For the natural fractures, a clear correlation between derived permeability, $k$, and accumulative shear displacement can not be identified. Instead, all results show a permeability increase, until, after the most significant slip, $d_{max}$, the permeability starts to decrease (Figure 7a). Notably, when $\sum d_i$ reaches a certain value (0.0445 mm for N03, 0.0570 mm for N21, and 0.0715 mm for N27), defined as the "critical shear displacement" here, the permeability also reaches its maximum value. There seems to be a positive relationship between the critical shear displacement and fracture roughness (Figure 7a). For the saw-cut fractures, the permeability of A28 (80 grit) also shows the same trend as observed for natural fractures, with a critical shear displacement of 0.0310 mm. Although Specimen A21 also displays a similar behavior to the natural fractures, its critical shear displacement is 0.0690 mm, which is much higher than expected. As for Specimen A34, its critical shear displacement may be lower than 0.0205 mm; which would provide a reasonable explanation for the permeability,$k_1$, decrease that occurred during the 1st slip event of saw-cut fractures. These findings indicate that there is a critical shear displacement, which corresponds to a certain roughness. When the accumulative

shear displacement exceeds this critical value, the fracture surface may have experienced substantial damage.

After the experiments, the specimens were removed from the pressure vessel and placed into tubes to rinse them with deionized water. Gouge material was found by visual examination for the natural fracture specimens, but not for the saw-cut specimens. All accumulative shear displacements, $\sum d_i$, recorded in this study are below 0.6 mm (Figure 7), which suggests that fracture surface asperities have experienced damage and formed gouge materials, which may clog the fracture and cause a decrease in permeability. For shear displacements below 1 mm, shear dilation has also not been immediately apparent in previous studies [31, 39]. Instead, contact area compression, caused by normal stress acting on the fracture surface and asperity damage caused by shear displacement, probably dominated the hydraulic aperture evolution.

We propose a potential mechanism to explain these complex phenomena, which is illustrated in Figure 8. Here, the full process of permeability evolution, dominated by shear displacement, can be divided into two stages. First, the permeability-increasing stage, where some major asperities dictate the fracture aperture for a given normal stress. After one or more triggered shear slip events, these asperities are damaged. Given the extremely small shear displacement, small apertures and low fluid velocities, the formed grains remain at or near their initial positions. For a given normal stress (a constant normal stress here), although these asperities are damaged, the fracture aperture does not change significantly. Instead, more flow paths can form during this stage, thereby increasing fracture permeability. The hypothesis about the damage of asperities is supported by the observed gouge material, found after the experiment, apparently caused by the shear displacement.

Next, the permeability-decreasing stage, results from the slip event with the largest shear displacement, $d_{max}$. As shear displacements accumulate further, the asperities are damaged and ground up, leading to the rearrangement and rotation of gouge material, which gradually blocks flow paths between the fracture surfaces. When asperities, on the fracture surface, rode up on each other (shear dilatancy), they became increasingly damaged, so that the contact area between the fracture surfaces increased, while the aperture decreased, which leads to permeability reduction. Meanwhile, the increase in fracture friction reduces the induced shear displacement, $d$, which is observed in Specimens N03 and N21. Certainly, the physical processes that took place in the fractures during slip events are highly complex and depend on fracture geometry as well as the slip history of the fracture surfaces, making it difficult to provide a general assessment of all competing processes

during these shear slip events.

## 5. Conclusions

We experimentally studied the fracture permeability evolution due to successive shear slip events, triggered by elevated fluid pressures. Experiments were carried out on six Grimsel granite specimens, three with natural fractures and three with saw-cut fractures.

For all specimens, the permeability, $k$, changes up to one order of magnitude after experiencing shear slips. No consistent increasing or decreasing trend of permeability evolution was observed, neither for a single slip event, nor for the entire experiment. For the majority of the specimens, permeability increased during the first few shear slip events, reaching a maximum permeability after a critical shear displacement was achieved (0.0445 mm for N03, 0.0570 mm for N21, 0.0715 mm for N27, and 0.0310 mm for A28), exhibiting a positive relationship with respect to fracture roughness. Generally, permeability then decreased with further slip events after a large, in most cases the largest, shear displacement.

Triggering pressure, $P_t$, is larger for natural fracture specimens than for saw-cut specimens, which is likely caused by the larger shear strength given by natural fractures. The triggering pressure, $P_t$, required to cause consecutive shear slip events increased with each slip event, which is more pronounced in natural fractures. However, the pressure difference between consecutive slip events became successively smaller with ongoing slip events. This observation suggests decreasing degrees of morphological surface modifications with progressive shear slip events.

We attribute the correlations between the evolution of permeability, slip displacement, and triggering pressure to the interplay between fracture shear dilation and associated fracture surface damage and gouge production. The two competing processes can plausibly reconcile the seemingly non-consistent trend in permeability evolution. In subsurface engineering applications, the hydraulic shearing process may occur multiple times during the entire life cycle of the reservoir. The assumption of permanent permeability enhancement after the initial stimulation is therefore questionable. Since this study was largely phenomenological, the complexity of fracture permeability evolution certainly warrants further quantification and more sophisticated physical models.

**Acknowledgements**

MOS thanks the Werner Siemens Foundation (Werner Siemens-Stiftung – WSS) for their endowment of the Geothermal Energy and Geofluids (GEG.ethz.ch) group at ETH Zurich (ETHZ), Switzerland. This work is supported by the National Natural Science Foundation of China (41877239), the China Scholarship Council (201806220196), and the program for Outstanding PhD candidate of Shandong University (201413170). We thank J. Ma, M. Lima and N. Knornschild for their patient help on conducting the experiments. We further thank S. Zhang for discussions on designing the experimental procedure.

## References

[1] J. W. Tester, B. Anderson, A. Batchelor, D. Blackwell, R. DiPippo, E. Drake, J. Garnish, B. Livesay, M. C. Moore, K. Nichols, et al., The future of geothermal energy: Impact of enhanced geothermal systems (egs) on the united states in the 21st century, Massachusetts Institute of Technology 209 (2006).

[2] F. Amann, V. Gischig, K. Evans, J. Doetsch, R. Jalali, B. Valley, H. Krietsch, N. Dutler, L. Villiger, B. Brixel, et al., The seismo-hydromechanical behavior during deep geothermal reservoir stimulations: open questions tackled in a decameter-scale in situ stimulation experiment, Solid Earth 9 (2018) 115–137.

[3] V. S. Gischig, D. Giardini, F. Amann, M. Hertrich, H. Krietsch, S. Löw, H. Maurer, L. Villiger, S. Wiemer, F. Bethmann, et al., Hydraulic stimulation and fluid circulation experiments in underground laboratories: Stepping up the scale towards engineered geothermal systems, Geomechanics for Energy and the Environment (2020) 100175.

[4] B. R. Scanlon, R. C. Reedy, J.-P. Nicot, Comparison of water use for hydraulic fracturing for unconventional oil and gas versus conventional oil, Environmental science & technology 48 (2014) 12386–12393.

[5] B. D. Lutz, A. N. Lewis, M. W. Doyle, Generation, transport, and disposal of wastewater associated with marcellus shale gas development, Water Resources Research 49 (2013) 647–656.

[6] S. Emberley, I. Hutcheon, M. Shevalier, K. Durocher, B. Mayer, W. Gunter, E. Perkins, Monitoring of fluid–rock interaction and co2 storage through produced fluid sampling at the weyburn co2-injection enhanced oil recovery site, saskatchewan, canada, Applied Geochemistry 20 (2005) 1131–1157.

[7] M. M. Grimm Lima, P. Schädle, C. P. Green, D. Vogler, M. O. Saar, X.-Z. Kong, Permeability impairment and salt precipitation patterns during $co_2$ injection into single natural fractures, Water Resources Research 56 (2020) e2020WR027213.

[8] W. L. Ellsworth, Injection-induced earthquakes, Science 341 (2013) 1225942.

[9] K. F. Evans, F. H. Cornet, T. Hashida, K. Hayashi, T. Ito, K. Matsuki, T. Wallroth, Stress and rock mechanics issues of relevance to hdr/hwr engineered geothermal systems: review of developments during the past 15 years, Geothermics 28 (1999) 455–474.

[10] K. Breede, K. Dzebisashvili, X. Liu, G. Falcone, A systematic review of enhanced (or engineered) geothermal systems: past, present and future, Geothermal Energy 1 (2013) 4.

[11] P. A. Witherspoon, J. S. Y. Wang, K. Iwai, J. E. Gale, Validity of cubic law for fluid-flow in a deformable rock fracture, Water Resources Research 16 (1980) 1016–1024.

[12] Y. W. Tsang, P. Witherspoon, Hydromechanical behavior of a deformable rock fracture subject to normal stress, Journal of Geophysical Research: Solid Earth 86 (1981) 9287–9298.

[13] R. W. Zimmerman, S. Kumar, G. S. Bodvarsson, Lubrication theory analysis of the permeability of rough-walled fractures, International Journal of Rock Mechanics and Mining Sciences and Geomechanics Abstracts 28 (1991) 325–331.

[14] R. W. Zimmerman, D.-W. Chen, N. G. Cook, The effect of contact area on the permeability of fractures, Journal of Hydrology 139 (1993).

[15] R. W. Zimmerman, G. S. Bodvarsson, Hydraulic conductivity of rock fractures, Transport in Porous Media 23 (1996) 1–30.

[16] I. W. Yeo, M. H. De Freitas, R. W. Zimmerman, Effect of shear displacement on the aperture and permeability of a rock fracture, International Journal of Rock Mechanics and Mining Sciences 35 (1998) 1051–1070.

[17] N. Watanabe, N. Hirano, N. Tsuchiya, Determination of aperture structure and fluid flow in a rock fracture by high-resolution numerical modeling on the basis of a flow-through experiment under confining pressure, Water Resources Research 44 (2008) n/a–n/a.

[18] K. Nemoto, N. Watanabe, N. Hirano, N. Tsuchiya, Direct measurement of contact area and stress dependence of anisotropic flow through rock fracture with heterogeneous aperture distribution, Earth and Planetary Science Letters 281 (2009) 81–87.

[19] D. Vogler, F. Amann, P. Bayer, D. Elsworth, Permeability evolution in natural fractures subject to cyclic loading and gouge formation, Rock Mechanics and Rock Engineering 49 (2016) 3463–3479.

[20] K. Iwai, Fundamental studies of fluid flow through a single fracture., PhD thesis - Berkeley: University of California (1976).

[21] M. Gutierrez, L. Øino, R. Nygaard, Stress-dependent permeability of a de-mineralised fracture in shale, Marine and Petroleum Geology 17 (2000) 895–907.

[22] D. Huo, S. Benson, Experimental investigation of stress-dependency of relative permeability in rock fractures, Transport in Porous Media 113 (2016).

[23] P. A. Selvadurai, S. D. Glaser, Laboratory-developed contact models controlling instability on frictional faults, Journal of Geophysical Research: Solid Earth 120 (2015) 4208–4236. 2014JB011690.

[24] D. Vogler, R. R. Settgast, C. Annavarapu, P. Bayer, F. Amann, Hydro-mechanically coupled flow through heterogeneous fractures, PROCEEDINGS, 42nd Workshop on Geothermal Reservoir Engineering, Stanford, CA SGP-TR-209 (2016b) 1–6.

[25] T. Kling, D. Vogler, L. Pastewka, F. Amann, P. Blum, Numerical simulations and validation of contact mechanics in a granodiorite fracture, Rock Mechanics and Rock Engineering (2018).

[26] D. Vogler, R. R. Settgast, C. Annavarapu, C. Madonna, P. Bayer, F. Amann, Experiments and simulations of fully hydro-mechanically coupled response of rough fractures exposed to high pressure fluid injection, Journal of Geophysical Research: Solid Earth 123 (2018) 1186–1200.

[27] N. Barton, S. Bandis, K. Bakhtar, Strength, deformation and conductivity coupling of rock joints, International Journal of Rock Mechanics and Mining Sciences 22 (1985) 121–140.

[28] N. G. W. Cook, Natural joints in rock - mechanical, hydraulic and seismic behavior and properties under normal stress, International Journal of Rock Mechanics and Mining Sciences and Geomechanics Abstracts 29 (1992) 198–223.

[29] J. Zhao, E. Brown, Hydro-thermo-mechanical properties of joints in the carnmenellis granite, Quarterly Journal of Engineering Geology and Hydrogeology 25 (1992) 279–290.

[30] S. Sisavath, A. Al-Yaarubi, C. C. Pain, R. W. Zimmerman, A simple model for deviations from the cubic law for a fracture undergoing dilation or closure, in: Thermo-Hydro-Mechanical Coupling in Fractured Rock, Springer, 2003, pp. 1009–1022.

[31] T. Esaki, S. Du, Y. Mitani, K. Ikusada, L. Jing, Development of a shear-flow test apparatus and determination of coupled properties for a single rock joint, International Journal of Rock Mechanics and Mining Sciences **36** (1999) 641–650.

[32] H. S. Lee, T. F. Cho, Hydraulic characteristics of rough fractures in linear flow under normal and shear load, Rock Mechanics and Rock Engineering 35 (2002) 299–318.

[33] H. Auradou, G. Drazer, A. Boschan, J.-P. Hulin, J. Koplik, Flow channeling in a single fracture induced by shear displacement, Geothermics 35 (2006) 576–588.

[34] Y. Fang, D. Elsworth, C. Wang, T. Ishibashi, J. P. Fitts, Frictional stability-permeability relationships for fractures in shales, Journal of Geophysical Research: Solid Earth 122 (2017) 1760–1776.

[35] Y. Fang, D. Elsworth, T. Ishibashi, F. Zhang, Permeability evolution and frictional stability of fabricated fractures with specified roughness, Journal of Geophysical Research: Solid Earth 123 (2018) 9355–9375.

[36] K. Im, D. Elsworth, Y. Fang, The influence of preslip sealing on the permeability evolution of fractures and faults, Geophysical Research Letters 45 (2018) 166–175.

[37] T. Ishibashi, D. Elsworth, Y. Fang, J. Riviere, B. Madara, H. Asanuma, N. Watanabe, C. Marone, Friction-stability-permeability evolution of a fracture in granite, Water Resources Research 54 (2018) 9901–9918.

[38] Q. Wenning, C. Madonna, T. Kurotori, R. Pini, Dataset-mapping fracture aperture changes with displacement, Journal of Geophysical Research: Solid Earth (2018).

[39] Q. C. Wenning, C. Madonna, T. Kurotori, R. Pini, Spatial mapping of fracture aperture changes with shear displacement using x-ray computerized tomography, Journal of Geophysical Research: Solid Earth 124 (2019) 7320–7340.

[40] D. Crandall, J. Moore, M. Gill, M. Stadelman, Ct scanning and flow measurements of shale fractures after multiple shearing events, International Journal of Rock Mechanics and Mining Sciences 100 (2017) 177–187.

[41] I. Faoro, A. Niemeijer, C. Marone, D. Elsworth, Influence of shear and deviatoric stress on the evolution of permeability in fractured rock, Journal of Geophysical Research: Solid Earth 114 (2009).

[42] W. Olsson, S. Brown, Hydromechanical response of a fracture undergoing compression and shear, International journal of rock mechanics and mining sciences & geomechanics abstracts 30 (1993) 845–851.

[43] W. Wu, J. S. Reece, Y. Gensterblum, M. D. Zoback, Permeability evolution of slowly slipping faults in shale reservoirs, Geophysical Research Letters 44 (2017) 11–368.

[44] Y. Jiang, B. Li, Y. Tanabashi, Estimating the relation between surface roughness and mechanical properties of rock joints, International Journal of Rock Mechanics and Mining Sciences 43 (2006) 837–846.

[45] L. P. Frash, J. W. Carey, Z. Lei, E. Rougier, T. Ickes, H. S. Viswanathan, High-stress triaxial direct-shear fracturing of utica shale and in situ x-ray microtomography with permeability measurement, Journal of Geophysical Research: Solid Earth 121 (2016) 5493–5508.

[46] Y. Ji, W. Wu, Z. Zhao, Unloading-induced rock fracture activation and maximum seismic moment prediction, Engineering Geology 262 (2019) 105352.

[47] M. O. Saar, M. Manga, Seismicity induced by seasonal groundwater recharge at mt. hood, oregon, Earth and Planetary Science Letters 214 (2003) 605–618.

[48] B. Figueiredo, C.-F. Tsang, J. Rutqvist, J. Bensabat, A. Niemi, Coupled hydro-mechanical processes and fault reactivation induced by co2 injection in a three-layer storage formation, International Journal of Greenhouse Gas Control 39 (2015) 432–448.

[49] D. Vogler, Hydro-mechanically coupled processes in heterogeneous fractures: experiments and numerical simulations, Ph.D. thesis, ETH Zurich, 2016.

[50] D. Vogler, S. D. C. Walsh, P. Bayer, F. Amann, Comparison of surface properties in natural and artificially generated fractures in a crystalline rock, Rock Mechanics and Rock Engineering 50 (2017) 2891–2909.

[51] D. Vogler, S. D. C. Walsh, E. Dombrovski, M. A. Perras, A comparison of tensile failure in 3d-printed and natural sandstone, Engineering Geology 226 (2017) 221–235.

[52] M. M. Grimm Lima, D. Vogler, L. Querci, C. Madonna, B. Hattendorf, M. O. Saar, X.-Z. Kong, Thermally driven fracture aperture variation in naturally fractured granites, Geothermal Energy 7 (2019) 1–28.

[53] J. Ma, L. Querci, B. Hattendorf, M. O. Saar, X.-Z. Kong, Toward a spatiotemporal understanding of dolomite dissolution in sandstone by $CO_2$-enriched brine circulation, Environmental Science & Technology 53 (2019) 12458–12466.

[54] J. Ma, L. Querci, B. Hattendorf, M. O. Saar, X.-Z. Kong, The effect of mineral dissolution on the effective stress law for permeability in a tight sandstone, Geophysical Research Letters 47 (2020) e2020GL088346.

[55] M. M. Grimm Lima, H. Javanmard, D. Vogler, M. O. Saar, X.-Z. Kong, Flow-through drying during $co_2$ injection into brine-filled natural fractures: A tale of effective normal stress, 2020.

[56] R. Olsson, N. Barton, An improved model for hydromechanical coupling during shearing of rock joints, International Journal of Rock Mechanics and Mining Sciences 38 (2001) 317–329.

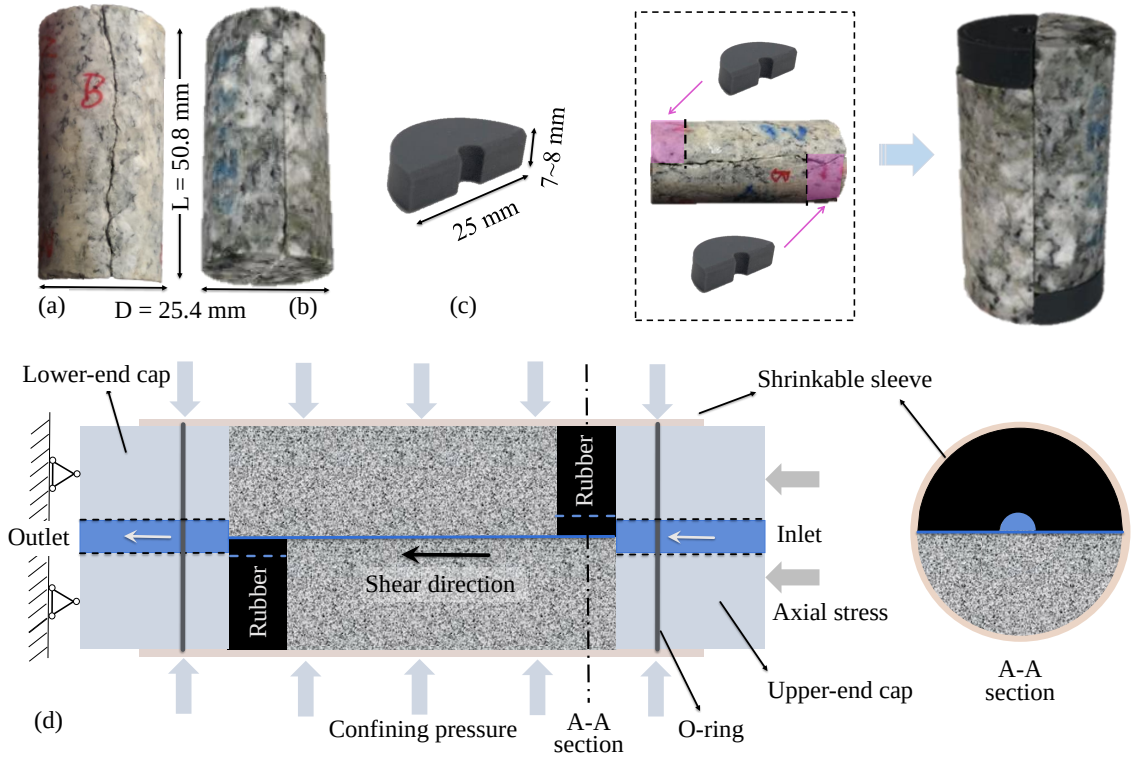


Figure 1: The instrumented specimen assembly consists of an upper end-cap, a lower end-cap, the fractured specimen, two black half-circle 3D printed rubber spacers, and a shrinkable sleeve, covering the specimen up to both end-caps. (a) Natural fracture; (b) saw-cut fracture; (c) 3D printed rubber spacer; (d) diagram of instrumented specimen.

Table 1: List of specimens and shear-flow experiment data summary

| Specimen No. | Fracture mode* | Slip event | Triggering pressure $P_t$ (MPa) | Slip displacement $d$ (mm) | Permeability** $k$ ($10^{-10}$m$^2$) |
|---|---|---|---|---|---|
| | | | Natural fracture | | |
| N03 | I/II | Pre-slip | - | - | 12.29 (±2.1972) |
| | | 1st | 0.734 | 0.0185 | 12.63 (±1.9075) |
| | | 2nd | 1.117 | 0.0260 | 20.57 (±2.9979) |
| | | 3rd | 1.403 | 0.0600 | 7.50 (±1.1461) |
| | | 4th | 1.596 | 0.0330 | 4.40 (±0.1191) |
| N21 | II | Pre-slip | - | - | 2.58 (±0.2765) |
| | | 1st | 1.890 | 0.0570 | 8.51 (±1.9186) |
| | | 2nd | 2.173 | 0.1890 | 4.09 (±1.8447) |
| | | 3rd | 2.354 | 0.1360 | 5.46 (±1.8630) |
| | | 4th | 2.516 | 0.1340 | 4.19 (±1.8471) |
| N27 | I | Pre-slip | - | - | 2.06 (±0.0114) |
| | | 1st | 1.380 | 0.0240 | 2.22 (±0.0090) |
| | | 2nd | 1.783 | 0.0475 | 4.74 (±0.6970) |
| | | 3rd | 2.144 | 0.1065 | 3.85 (±0.6310) |
| | | 4th | 2.394 | 0.2775 | 1.72 (±0.0715) |
| | | | Saw-cut fracture | | |
| A28 | 80 | Pre-slip | - | - | 1.65 (±0.0146) |
| | | 1st | 0.467 | 0.0310 | 3.70 (±0.2453) |
| | | 2nd | 0.591 | 0.0150 | 3.46 (±0.2856) |
| | | 3rd | 0.700 | 0.0155 | 2.96 (±0.2089) |
| | | 4th | 0.805 | 0.0175 | 2.45 (±0.1954) |
| A21 | 240 | Pre-slip | - | - | 1.09 (±0.0122) |
| | | 1st | 0.499 | 0.0385 | 1.06 (±0.0050) |
| | | 2nd | 0.692 | 0.0160 | 1.18 (±0.0243) |
| | | 3rd | 0.842 | 0.0145 | 3.24 (±0.6599) |
| | | 4th | 0.931 | 0.0140 | 1.80 (±0.0382) |
| A34 | 400 | Pre-slip | - | - | 8.17 (±0.0754) |
| | | 1st | 0.539 | 0.0205 | 1.48 (±0.0053) |
| | | 2nd | 0.728 | 0.0175 | 1.48 (±0.0053) |
| | | 3rd | 0.841 | 0.0155 | 1.37 (±0.0030) |
| | | 4th | 0.952 | 0.0140 | 1.48 (±0.0055) |

*Fracture modes are detailed as Mode I (tensile), Mode II (shear) or Mode I/II (tensile with partial shear) [19, 24, 49], while the fracture modes for the saw-cut specimens are given with respect to their grit.

**Permeability, $k$, is the average of the measured data and its fluctuation is quantified by the standard deviation shown in parentheses.

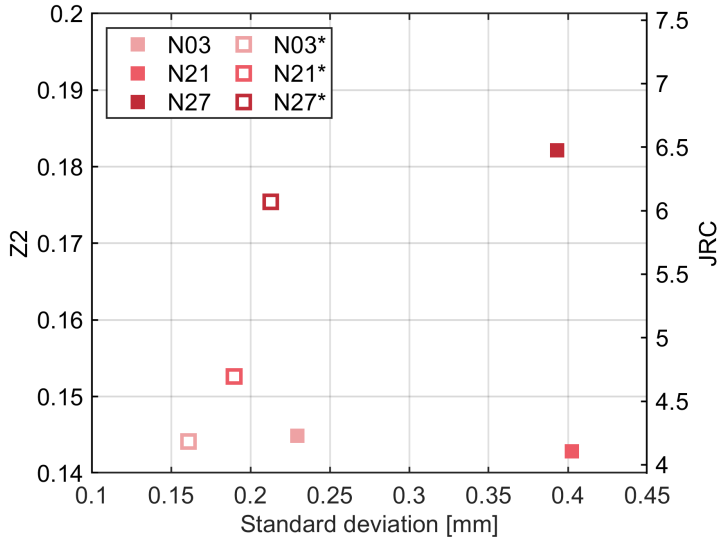


Figure 2: Fracture roughness of natural specimens. Solid markers indicate the standard deviation of the roughness vs. JRC and Z2 for the entire fracture surfaces. Surface roughness was also computed on 20 patches of 1 cm×1 cm, and the values were subsequently averaged and are denoted with an open marker.

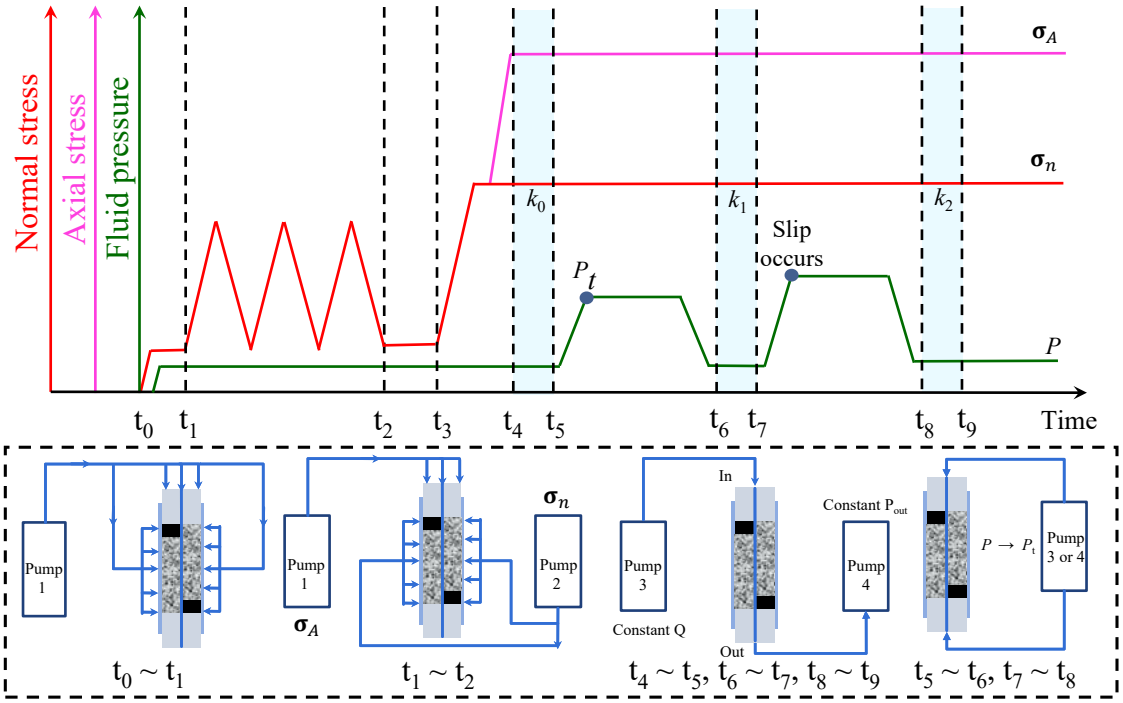


Figure 3: A diagram of the loading path along the time steps from $t_0$ to $t_9$. During $t_0 - t_1$, a normal stress and fluid pressure is applied to check the seal of the experimental setup. During $t_1 - t_2$, an initial loading is applied to ensure that the fracture is well mated. During $t_3 - t_4$, the axial stress and normal stress are increased. During $t_4 - t_5$, the 'starting' permeability, $k_0$, before the first shear slip event is calculated. During $t_5 - t_6$, the fluid pressure is increased until shear slip occurs, while the fluid pressure is kept constant until the shear displacement stops natural, then the fluid pressure is decreased. During $t_6 - t_7$, the permeability, $k_1$, is calculated after the shear slip event. After $t_7$, the process during $t_5 - t_7$ are repeated several times.

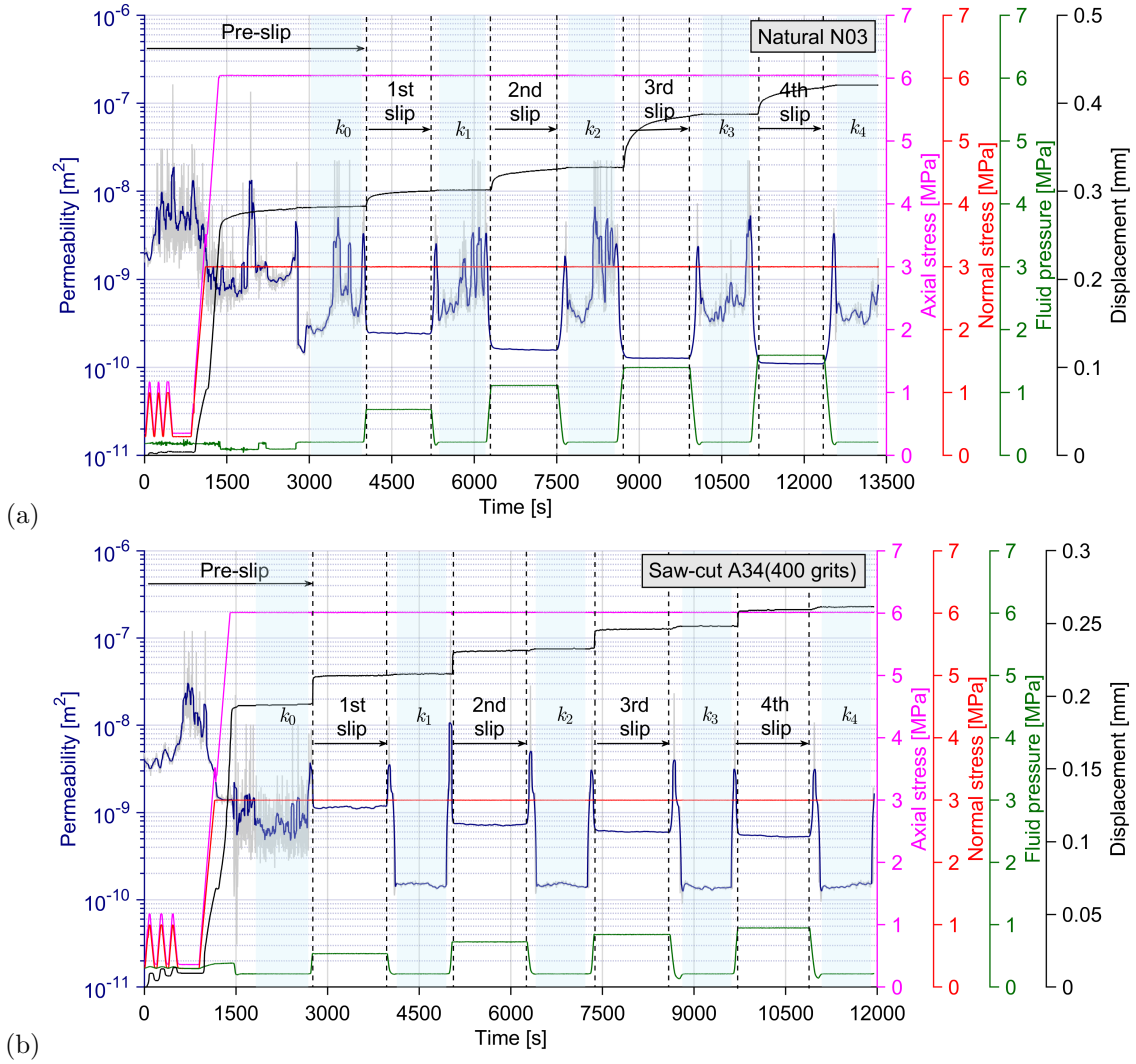


Figure 4: Loading path, accumulated displacement (since the start of the experiment) and calculated permeability (original data in gray and filtered data in dark blue) of specimens: (a) N03; and (b) A34. The range of shear displacements are marked with dotted lines. The permeability curve is obtained with automatically measured data by Eq. 1. However, permeability measurements under stationary conditions are only performed before and after individual slip events for about 15 minutes (light blue areas) due to the experimental setup.

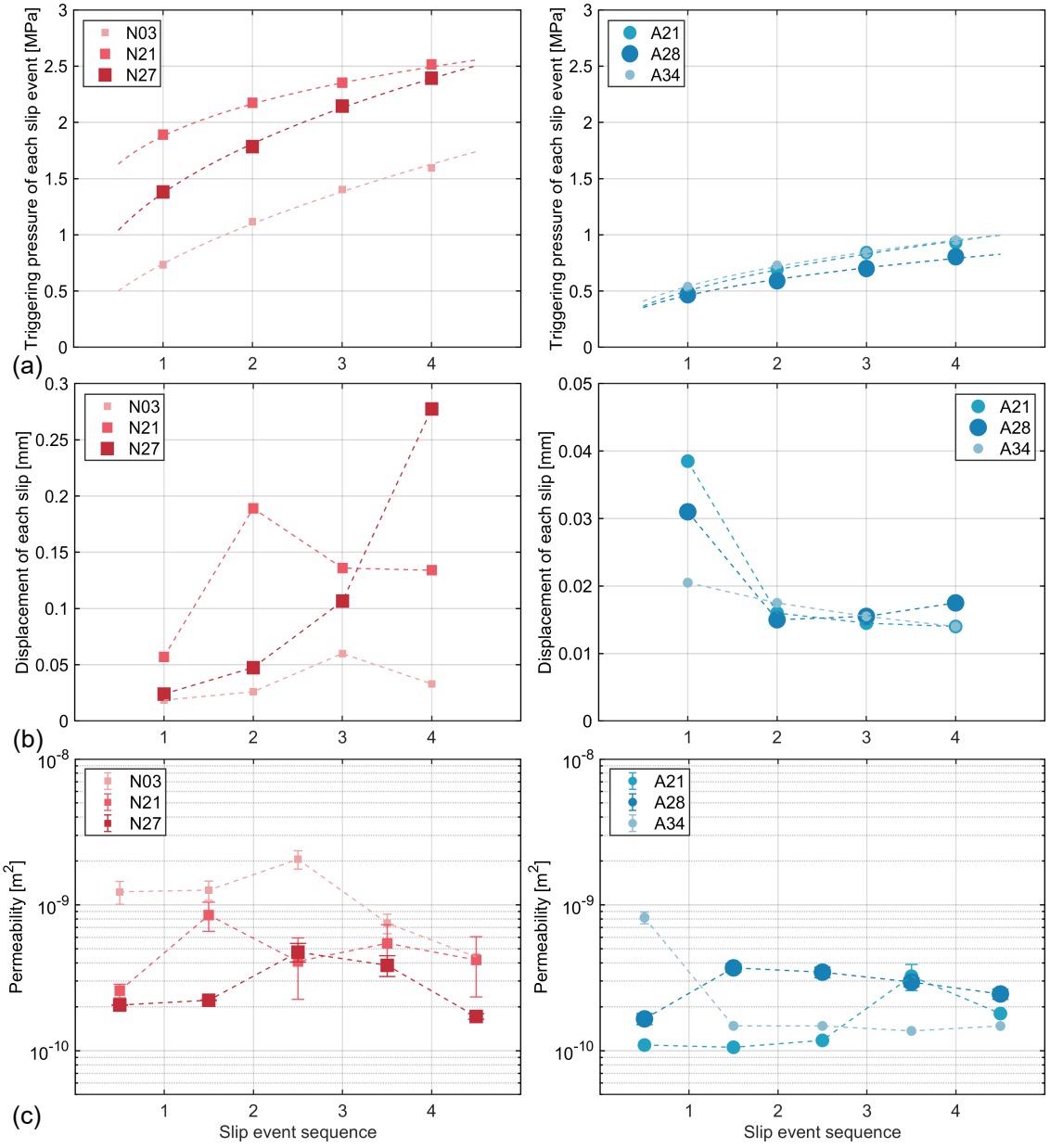


Figure 5: Experiment results of natural specimens and saw-cut specimens. (a) triggering pressure, $P_t$, (b) shear displacement, $d$, and (c) calculated permeability, $k$. A vertical error bar, representing the standard deviation, is plotted for each $k$ value, indicating the fluctuation of measured permeabilities. The trend of triggering pressure, $P_t$, versus slip event sequence is fitted with a power law. Specimens with larger roughness values are given by a bigger marker.

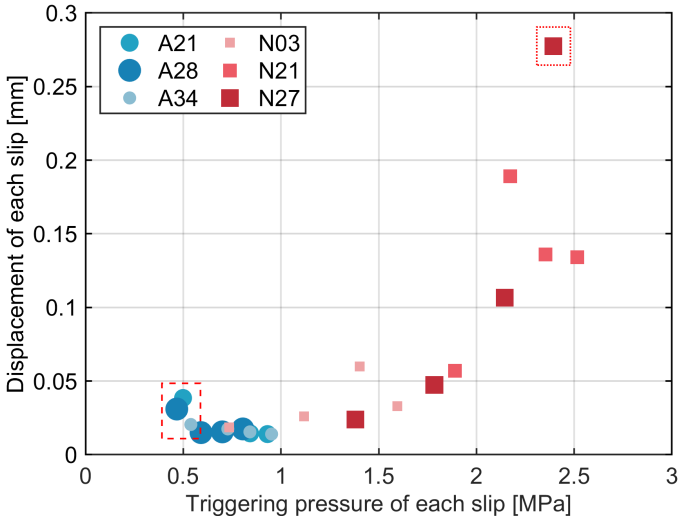


Figure 6: Relationship between triggering pressure, $P_t$, and shear displacement for each slip distance, $d$. The red box on the left marks the largest displacements of saw-cut fractures. The red box in the top right corner marks the largest shear displacement of Specimen N27, which shows a different evolution tendency compared to other natural specimens. Specimens with larger roughness values are marked by bigger markers.

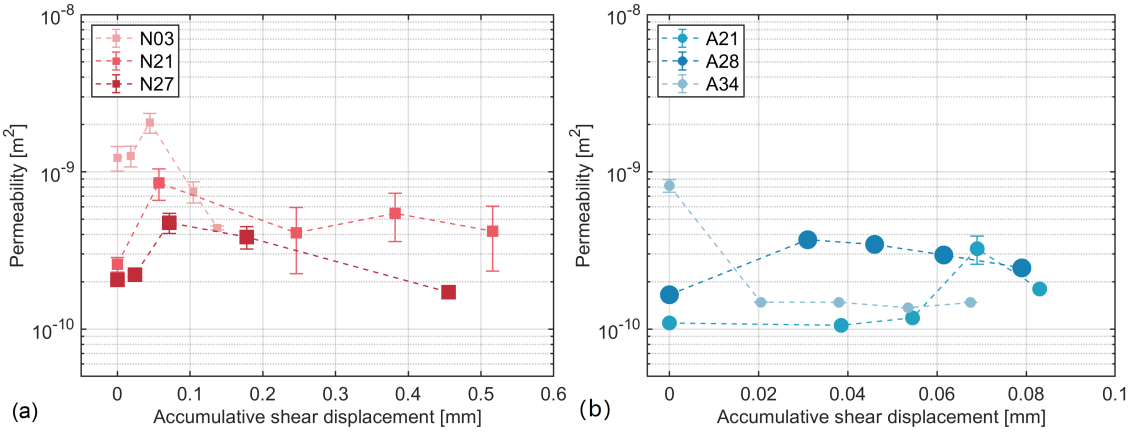


Figure 7: Relationship between calculated permeability, $k$, and accumulated shear displacement, $\sum d_i$ for (a) natural and (b) saw-cut fractures. The fluctuations in measured permeabilities, indicated by the vertical error bar, given as standard deviation. Note the different scale of the accumulative shear displacements for natural and saw-cut fractures. Specimens with larger roughness values are marked by bigger markers.

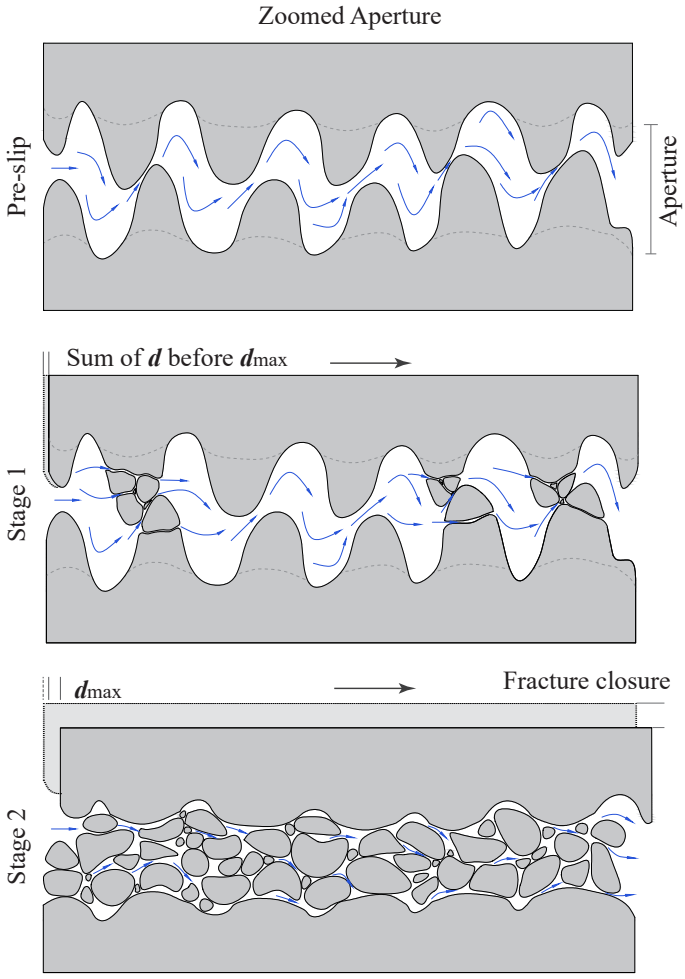


Figure 8: Conceptual model for the mechanism of permeability evolution (inspired by [34]). In an unaltered fracture aperture field, the dominating asperities determine the fracture permeability. During stage 1, the dominating asperities are damaged after the critical shear displacement (sum of $d$ before $d_{max}$). However, the newly formed grains are not redistributed significantly within the fracture yet, but produce more flow paths, resulting in permeability enhancement. During stage 2, after experiencing the largest shear displacement, $d_{max}$, the contact area changes and the aperture becomes increasingly smaller (fracture closure), which reduces permeability.

## Appendices

*Appendix A*

The JRC value has an implicit associated scale, as the JRC value is determined by comparing specimens with a length of 10 cm to a hierarchy of 'characteristic' surface proles [27]. Nevertheless, the arbitrary nature of this comparison makes the JRC value a somewhat qualitative measure of roughness. Thus, instead the Z2 measure is chosen. The dimensionless Z2 roughness measure is dened as:

$$Z2 = [\frac{1}{L}\int_0^L (\frac{dz}{dx})^2)dx]^{1/2}, \tag{A1}$$

where $z(x)$ is the prole height of the fracture surface. In practice, the Z2 value is determined from a discretization of the surface prole

$$Z2 = [\frac{1}{L}\sum \frac{(z_{i+1} - z_i)^2}{x_{i+1} - x_i}]^{1/2}, \tag{A2}$$

where $x_i$ and $z_i$ are the coordinates of the fracture surface, typically taken at regular sampling intervals, $\Delta x$, such that $x_{i+1} - x_i = \Delta x$ for all $i$ and $L$ is the total length of a scan line along which Z2 is measured. For reference, the corresponding JRC values was also obtained. For this paper, a sampling interval of 0.25 mm was used to determine all Z2 values, and the JRC value was then determined from:

$$JRC = 60.32(Z2) - 4.51, \tag{A3}$$

The dependency of the standard deviation on specimen size is removed by subsampling the standard deviation of the surface asperity heights within regions of fixed size at 20 randomly chosen locations on the surfaces.

*Appendix B*

The results of other natural specimens and saw-cut specimens are presented in Figures B1 and B2, respectively. For Specimens N21 and A21, the displacement is very large during the first mating cycle, which means that the mating of the specimen before the experiment setup was not as good as for the other four samples. The observation, once again, showcases the importance of performing mating cycles before testing.

For natural specimens, Figures 4 and B1 show that the slip rates of each sample were different. From a qualitative perspective, time passed before induced shear displacement increased in the order

of N27, N21, and N03, with the same order of specimens being observed for the fracture roughness. The same phenomenon, although more distinct, was also observed in saw-cut fractures (Figures 4 and B2). This implies that the required time to induce shear slip has a positive correlation with fracture roughness, because a rougher fracture requires more energy for initial shear slip.

Another observation is that all permeability measurements, $k$, display different levels of fluctuation during the measurement window, which is quantified by the standard deviation (Table 1) and plotted as error bars in Figure 5c. Notably, larger permeabilities correspond to larger fluctuations for natural specimen, although permeability and permeability fluctuations decrease after $d_{max}$. This indicates two points, the hydraulic aperture became smaller, and the damage of asperities changes flow paths significantly. No clear indications are found about the relationship between the roughness and fluctuation for natural fractures. For the saw-cut specimens, the fluctuation increases with fracture roughness. As to the fluctuation trend of $k$, there is no correlation between the permeability and its fluctuation in either natural specimens or saw-cut specimens, because the surface geometry is different for each specimen.

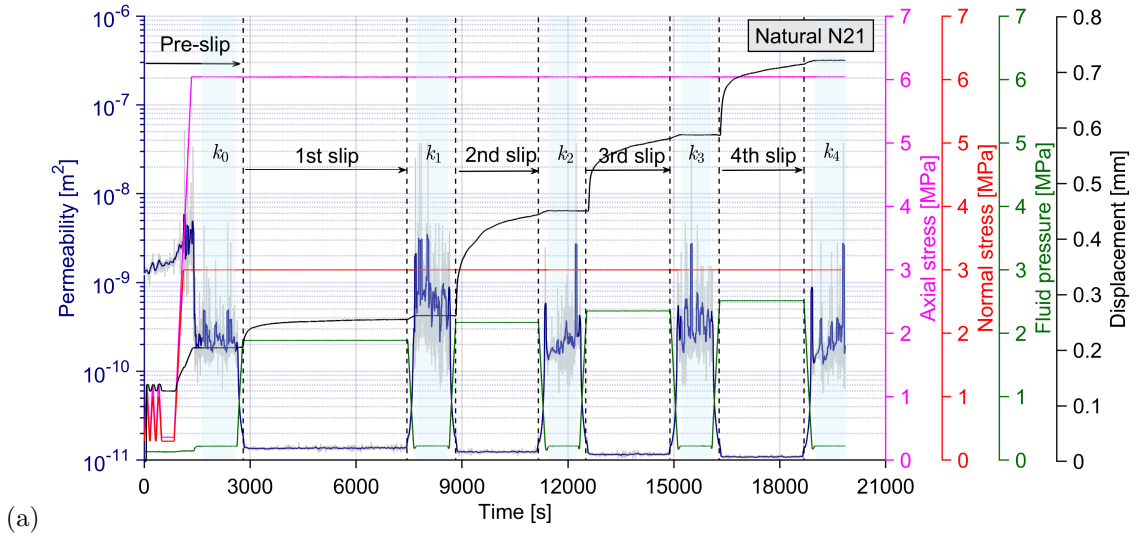


(a)

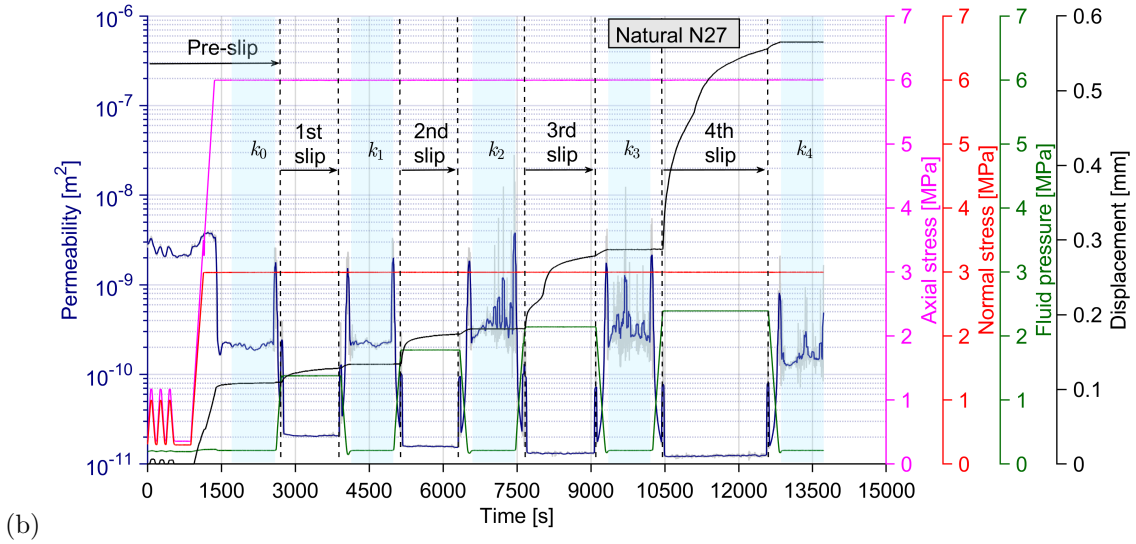


(b)

Figure B1: Loading path, accumulated displacement (since the start of the experiment) and calculated permeability of specimens: (a) N21 and (b) N27.

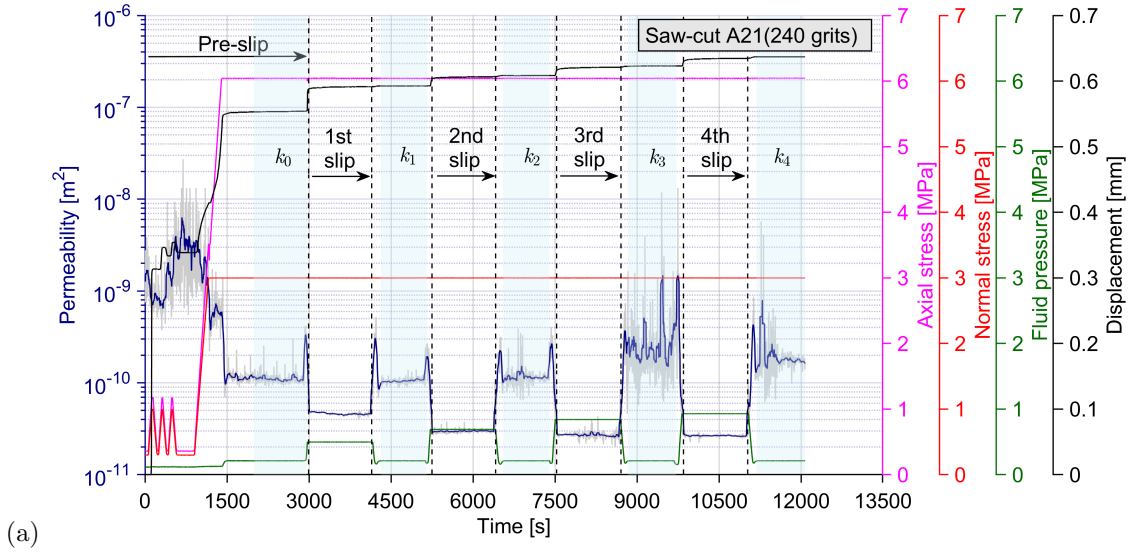


(a)

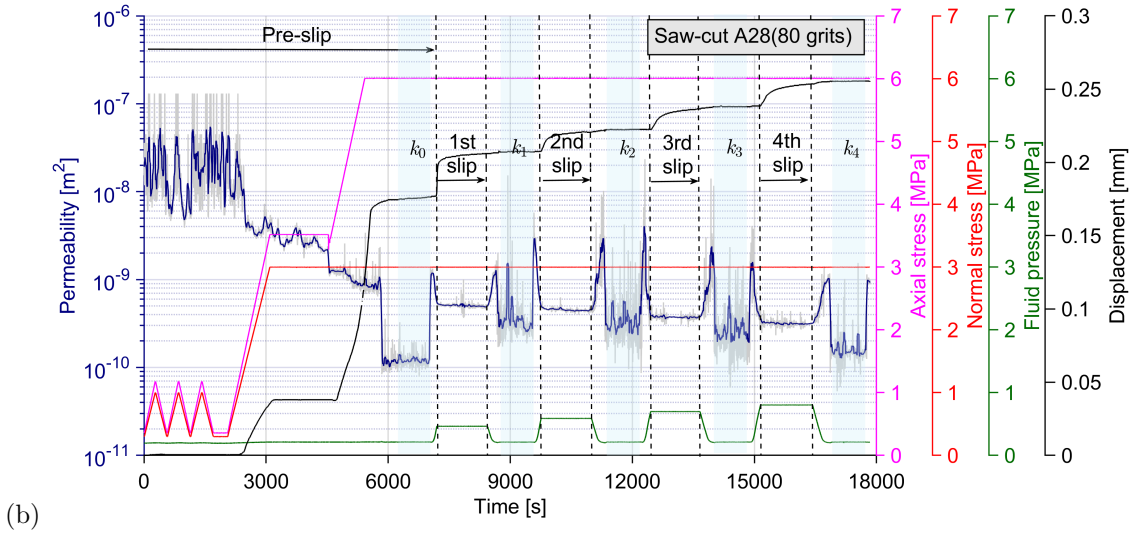


(b)

Figure B2: Loading path, accumulated displacement (since the start of the experiment) and calculated permeability of specimens: (a) A21 and (b) A28.